Engineering xxx (xxxx) xxx

Contents lists available at ScienceDirect

Engineering

journal homepage: www.elsevier.com/locate/eng

Research
Advanced Antennas for Wireless Connectivity—Article

High-Efficiency Circularly Polarized Phased Array Based on 5 μm-Thick Nematic Liquid Crystals: Design, Over-The-Air Calibration, and Experimental Validation

Xin Yu Wu [a], Fengshuo Wan [a], Hongyuan Feng [a], Shichao Jin [b], Chong Guo [a,c], Yu Wei [a], Dunge Liu [b], Yuqian Yang [b], Longzhu Cai [a,c], Zhi Hao Jiang [a,c,*], Wei Hong [a,c]

[a] State Key Laboratory of Millimeter Waves, School of Information Science and Engineering, Southeast University, Nanjing 210096, China
[b] State Key Laboratory of Space–Ground Integrated Information Technology, Beijing Institute of Satellite Information Engineering, Beijing 100095, China
[c] Research Institute of Millimeter-Wave and Terahertz Technology (RIMMATT), Nanjing 211111, China

ARTICLE INFO

Article history:
Available online xxxx

Keywords:
Circularly polarized
Liquid crystal
Liquid crystal-based phased array (LCPA)
Phase shifter
Over-the-air (OTA) calibration

ABSTRACT

This paper presents a systematic investigation and demonstration of a K-band circularly polarized liquid-crystal-based phased array (LCPA), including the design, over-the-air (OTA) in-array calibration, and experimental validation. The LCPA contains 16 phase-shifting radiating channels, each consisting of a circularly polarized stacked patch antenna and a liquid-crystal-based phase shifter (LCPS) based on a loaded differential line structure. Thanks to its slow-wave properties, the LCPS exhibits a maximum phase-shifting range of more than 360° with a figure of merit of 78.3°·dB^{-1} based on a liquid crystal layer with a thickness of only 5 μm. Furthermore, an automatic OTA calibration based on a state ergodic method is proposed, which enables the extraction of the phase–voltage curve of every individual LCPA channel. The proposed LCPA is manufactured and characterized with a total profile of only 1.76 mm, experimentally demonstrating a scanned circularly polarized beam from −40° to +40° with a measured peak gain of 12.5 dBic and a scanning loss of less than 2.5 dB. The bandwidth of the LCPA, which satisfies the requirements of port reflection ($|S_{11}|$) < −15 dB, an axial ratio (AR) < 3 dB, beam squinting < 3°, and a gain variation < 2.2 dB, spans from 25.5 to 26.0 GHz. The total efficiency is about 34%, which represents a new state of the art. The use of the demonstrated low-profile LCPA to support circularly polarized scanning beams, along with the systematic design and calibration methodology, holds potential promise for a variety of millimeter-wave applications.

1. Introduction

With the commercialization of 5G communications [1] and the development of the Internet of Things [2], planar antenna arrays supporting electronically scanned beams are indispensable components that are widely employed in wireless systems for a variety of applications such as communications, radars, sensing, and imaging [3]. Conventional approaches to realize electronically scanned arrays rely on the usage of a large number of beamforming circuits/chips with high cost and high complexity [4,5]. Thus, alternative new array technologies that can accomplish such functionalities have been actively sought over the past few decades. These emerging methods either utilize reconfigurable components, such as varactor diodes [6,7], positive-intrinsic-negative (PIN) diodes [8], and micro-electro-mechanical systems (MEMS) switches [9,10], or exploit phase-change materials, such as ferroelectric materials [11], barium strontium titanate (BST) films [12], and liquid crystals (LCs) [13], to achieve the tunable phase delays required for dynamically controllable beamforming. Among these methods, LCs are of particular interest due to their low cost and maturity for mass production, which have already been demonstrated in the display industry [14–16]. An LC is a state of matter partway between a crystalline solid and an amorphous liquid; one of the most common phases of an LC is the nematic phase [17]. Nematic LCs inherently exhibit uniaxial electromagnetic responses and own an electrical tunable permittivity. As a result, they have attracted a tremendous amount of interest in the field of microwave engineering, in applications such as phase shifters [18–20], filters [21,22], polarization agile antennas [23],

* Corresponding author.
E-mail address: zhihao.jiang@seu.edu.cn (Z.H. Jiang).

https://doi.org/10.1016/j.eng.2023.08.013

Please cite this article as: X.Y. Wu, F. Wan, H. Feng et al., High-Efficiency Circularly Polarized Phased Array Based on 5 μm-Thick Nematic Liquid Crystals: Design, Over-The-Air Calibration, and Experimental Validation, Engineering, https://doi.org/10.1016/j.eng.2023.08.013

and multi-mode antennas [24]. In particular, LC-based beam-steering antennas [13,16,23–36] have become a promising technological venue for a number of applications and have thus been widely studied. Compared with beam-steering antennas based on existing reconfigurable components [6–10], LC-based beam-steering antennas have the advantages of a lower cost, better integration, and/or continuous tunable phases. Moreover, in contrast to other phase-change materials [11,12] used for beam-scanning antennas, LC materials allow for a wider operational frequency range from microwaves to terahertz, while requiring lower bias voltages. The previously reported beam-steering antennas based on LCs can be further divided into LC-based lens antennas [25,26], LC-based leaky wave antennas [16,27], LC-based reflectarrays [28–30], and LC-based phased arrays (LCPAs) [13,31–36]. Among these, LCPAs are relatively more promising candidates for potential applications due to their low profile and ease of integration.

Over the past few years, various types of LCPAs have been investigated, with a typical architecture containing multiple channels, each including a radiating element and an LC-based phase shifter (LCPS). Different types of radiators have been used for the array element, such as magneto-electric dipoles [31], patches [13,33], dielectric resonator antennas [34], and Yagi-Uda antennas [35]. An LCPS usually adopts LCs as the substrate material and provides tunable phases with a resonant or non-resonant structure; a commonly used structure is the LC-loaded inverted microstrip line (IMSL) [13,19,20,33–35]. As described in Ref. [31], it demonstrates a Ka-band 1×4 LCPA constructed with planar magnetoelectric dipoles and reflection-type LCPSs based on a 127 μm-thick LC layer. This LCPA achieves a maximum gain of 6.7 dBi with a small scanning coverage from −22° to +23°. Another reported K-band 2×2 LCPA adopts a single-layer patch as the array element and a 127 μm-thick LC layer as the substrate of an IMSL LCPS [13]. Since the two-dimensional (2D) array arrangement is realized by using miniaturizedradiators and phase shifters, the LCPA suffers from a relatively small scanning range of less than ±23° and a gain of only 5.9 dBi. As described in Ref. [35], it proposes a 1×4 endfire LCPA based on Yagi-Uda elements. The thickness of the LC layer of the LCPS is reduced to 20 μm, while the beam can be scanned from −40° to +40°. However, only a maximum gain of 4.9 dBi is achieved, due to the thin LC layer. This structure is further modified by combining the LCPSs with a Butler matrix [37], which enhances the scanning range and gain to ±60° and 5.8 dBi at the expense of using a more complicated circuitry.

In addition to depending on the LCPA's structural design, the performance of an LCPA strongly relies on the fabrication capability, especially the LC filling technology [14]. In general, a fully closed cavity between the substrates is required to contain the LC molecules; this can be realized by hollowing out a portion of the printed circuit boards (PCBs) [31], removing parts from the metallic plates [33], or separating two layers of glass with surrounding spacers [13]. The thickness and filling accuracy of the LC layer will directly affect the channel uniformity and switching time of the LCPA. It can be seen from the previously reported LCPA designs that several shortcomings still need to be overcome. First, it is desirable to extend the radiation polarization of LCPAs—which has been limited to linear polarization—into circular polarization for applications such as satellite communications and radar imaging. Second, almost all existing LCPAs have a small number of array elements (i.e., no more than four), resulting in the disadvantages of a very limited gain and a low beam resolution. Third, the majority of the LCPAs reported thus far possess an LC layer thickness greater than 20 μm; however, thinner LC layers are called for in order to reduce the beam-switching time and material cost.

Another urgent challenge to be solved is the development of a reliable calibration method for LCPAs. Unlike phased arrays that are based on digital phase shifters with discretized phase shifting, LCPSs provide continuously tunable phases by rotating the LC molecules with different bias voltages. Importantly, the relationship between the transmission phase and the bias voltage—that is, the phase–voltage curve—needs to be experimentally determined for accurate beamforming. Due to this unknown phase–voltage relationship, conventional calibration methods are no longer suitable, including the rotating-element electric-field vector (REV) method [38,39], phase-toggling method [40], or synthetic array calibration [41]. Moreover, inaccuracy of the geometrical dimensions and fluctuation of the material properties of the LCPSs can lead to performance variation, including in both the initial phase and the line shape of the phase–voltage curve, particularly for LCPAs based on an ultrathin LC layer. Thus, all the channels of the LCPA must be individually calibrated by determining the distinct phase–voltage curve for each channel.

Although several calibration methods for LC-based antennas have been proposed, they have significant limitations. One approach is to measure the phase–voltage curve of every employed LCPS without being connected to the radiating element [36]. This method is cumbersome and is only suitable for small-scale LCPAs; thus, it cannot be applied to millimeter-wave LCPAs with seamlessly connected radiating elements and LCPSs. Another method is to measure a separate LCPS and use its phase–voltage curve for all the channels in the LCPA for beamforming [35]. However, this method ignores the differences between different channels. To date, there is still a lack of an over-the-air (OTA) in-array calibration method for extracting the characteristics of each channel in an LCPA; nevertheless, this information is indispensable and critical, especially for LCPAs with a large array size and a thin LC layer (e.g., when the thickness of the LC layer is less than 10 μm).

In this paper, a systematic design, OTA calibration, and experimental validation of a circularly polarized (CP) phased array operating in the K-band based on 5 μm-thick ultrathin LCs are proposed. The LCPA contains 16 phase-shifting radiating channels, each consisting of a CP stacked patch antenna and a novel LCPS. Based on a differential line structure with periodic metallic bar loadings, the proposed LCPSs offer a phase-shifting range of more than 360° and a figure of merit (FoM) of $78.3°\cdot dB^{-1}$ with an LC layer only 5 μm thick. Moreover, a novel OTA calibration strategy based on the state ergodic method (SEM) is proposed and implemented to automatically extract the phase–voltage curves of each channel in the LCPA. Finally, by applying a phase assignment strategy to the extracted phase–voltage curves, high-performance beam steering can be achieved, which is experimentally demonstrated with a scanned CP beam from −40° to +40° within a frequency range from 25.5 to 26.0 GHz, with a maximum gain of 12.5 dBic and a total efficiency of about 34%. The proposed generic methodology paves the way for the design and characterization of LCPAs for communications and sensing; it can also be applied to different forms of beam-scanning arrays based on LCs or even other types of phase-change materials. The advantages of the proposed LCPA include its high efficiency, low profile, and faster response time. The current one-dimensional (1D) beam-scanning ability can be useful in vehicular communication, assembly line monitoring, geological detection, and other applications. By expanding the array scale and extending the arrays to 2D arrays, high-gain and 2D beam-scanning properties can be achieved with a low manufacturing cost, holding promise for a broad range of millimeter-wave applications such as satellite communications, radars, and imaging.

2. Design of the LCPA

The schematic diagram of the LCPA sub-system is displayed in Fig. 1. The essence of the LCPA's beam-scanning capability relies

on the tunable phase shifts of each channel when different voltages are applied to the nematic LC molecules in the LCPSs. The entire LCPA sub-system includes the LCPSs, CP array elements, feeding network, and control board. The control board is used to adjust the LC states in each LCPS by providing desirable voltages according to the commands issued from a personal computer (PC). The designs of all the modules are described individually below.

2.1. Design of the LCPSs

As critical components in achieving beamforming for the LCPA, the design of the LCPSs is of great importance in realizing a full 360° phase coverage with a low insertion loss. Considering the limited available channel space and fabrication technology, the currently widely used IMSLs suffer from a small tunable phase coverage and high insertion loss [13,19,33–35]. To address this issue, a periodically loaded differential line (LDL) is employed, which enables an ultrathin LC thickness of less than 5 μm and a high FoM of the phase shifter.

2.1.1. Structure and modeling of the LCPSs

The configuration of the proposed LCPSs is depicted in Figs. 2(a)–(d). In the top view of the LCPS shown in Fig. 2(a), two microstrip lines are printed on the top layer of substrate 1 (TLY-5 with a thickness of 0.25 mm) in order to connect to the end launch-connectors for the scattering parameter characterization. The microstrip lines are coupled to the embedded microstrip lines, which are printed on the bottom layer of the top glass panel, through a slot etched out on the ground plane printed on the bottom layer of substrate 1. As shown in the bottom view of the LCPS (Fig. 2(b)), the main components of the LCPS include two baluns, two impedance-matching LDL transition sections, and an LDL phase-shifting section. The detailed structure of the differential line transition section with non-uniform loading is illustrated in the enlarged view (Fig. 2(c)), where the floating metallic bars printed on the top layer of the bottom glass panel are aligned perpendicularly to the differential line. For impedance matching, the lengths of the metallic bars are gradually reduced from the center to two ends. Indium-tin oxide (ITO) lines are connected to the differential line and metallic bars, respectively, for biasing. When a bias voltage (V_{bias}) is applied to the LCPS, the LCs in the overlapped area between the differential line and the metallic bars will exhibit a tunable permittivity value, whereas the properties of the LCs in the other regions will remain almost unchanged. The LCs in these two different types of regions are denoted as the effective LC and constant LC, respectively (see side view in Fig. 2(d)). The parameters of the LC material are the relative permittivity parallel to the long axis of the LC moleculars $\varepsilon_{//} \approx 3.84$, $\tan\delta_{//} \approx 0.007$, the relative permittivity orthogonal to the long axis of the LC moleculars $\varepsilon_{\perp} \approx 2.66$, and $\tan\delta_{\perp} \approx 0.015$, where $\tan\delta_{//}$ and $\tan\delta_{\perp}$ are the loss tangent values parallel and orthogonal to the long axis of the LC moleculars.

In order to clarify the working principle of the LCPS based on the periodically LDL, the equivalent circuit and the dispersion curves of a single unit cell with and without the metallic bar loading are illustrated in Fig. 2(e). The equivalent circuit of the unloaded differential line, which is a transverse electromagnetic transmission line, is composed of a series inductor (L_0) and a parallel capacitor (C_0) that are almost constant and unaffected by the LC states [20], as manifested by the dispersion curves (see the dot-dash lines in Fig. 2(f)). After loading the metallic bars, an extra shunt inductor (L_{bar}) is introduced, along with two series-connected shunt capacitors (C_{LC}) formed in the overlapped regions between the bars and the differential line. The dispersion curves of the unit cell with and without the bar loading obtained by a full-wave eigenmode solver are displayed in Fig. 2(f). It can be seen that the loaded unit cells exhibit the characteristics of slow-wave structures [42]. When increasing the permittivity value of the LCs, the dispersion curves of the unloaded differential line remain almost unchanged; in contrast, a phase difference of 10.8° occurs in the LDL across a single unit cell at 25.5 GHz. From the vectorial of the electric field in Fig. 2(g), it can be seen that the fields of the LDL structure are strongly bounded in the overlap areas, revealing that the effective permittivity is mainly controlled by the 5 μm-thick LC layer instead of the glass substrates. Since a thinner LC layer can result in a larger C_{LC}, a wide variation range in ΔC_{LC} can be achieved by modifying the permittivity value of the 5 μm-thick LC material. Correspondingly, the propagation constant β can also be changed to realize the phase-shifting function of the unit cell. In our design, the number of unit cells is selected to be 41 in order to achieve a smaller size and a lower insertion loss, on the premise of reaching a phase-shifting range of 360°.

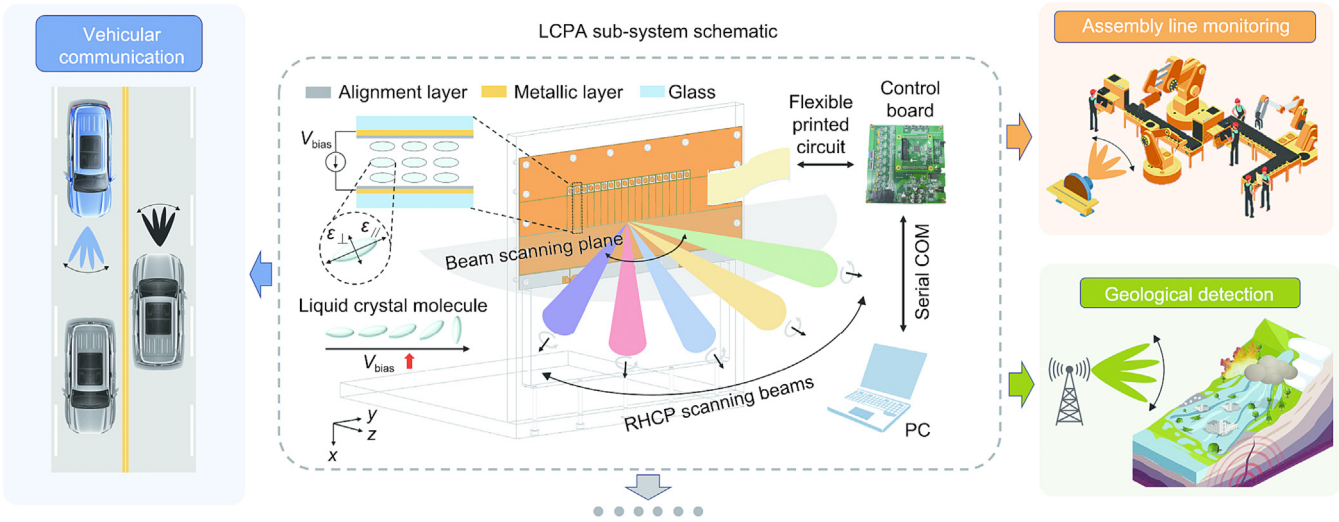

Fig. 1. Schematic diagram and application scenarios of the proposed K-band circularly polarized LCPA sub-system. PC: personal computer; RHCP: right-handed circularly polarized; COM: communication; V_{bias}: bias voltage; $\varepsilon_{//}$ and $\varepsilon_{\perp}$: the relative permittivity parallel and orthogonal to the long axis of the LC moleculars; x, y, z: the axes of the Cartesian coordinate system.

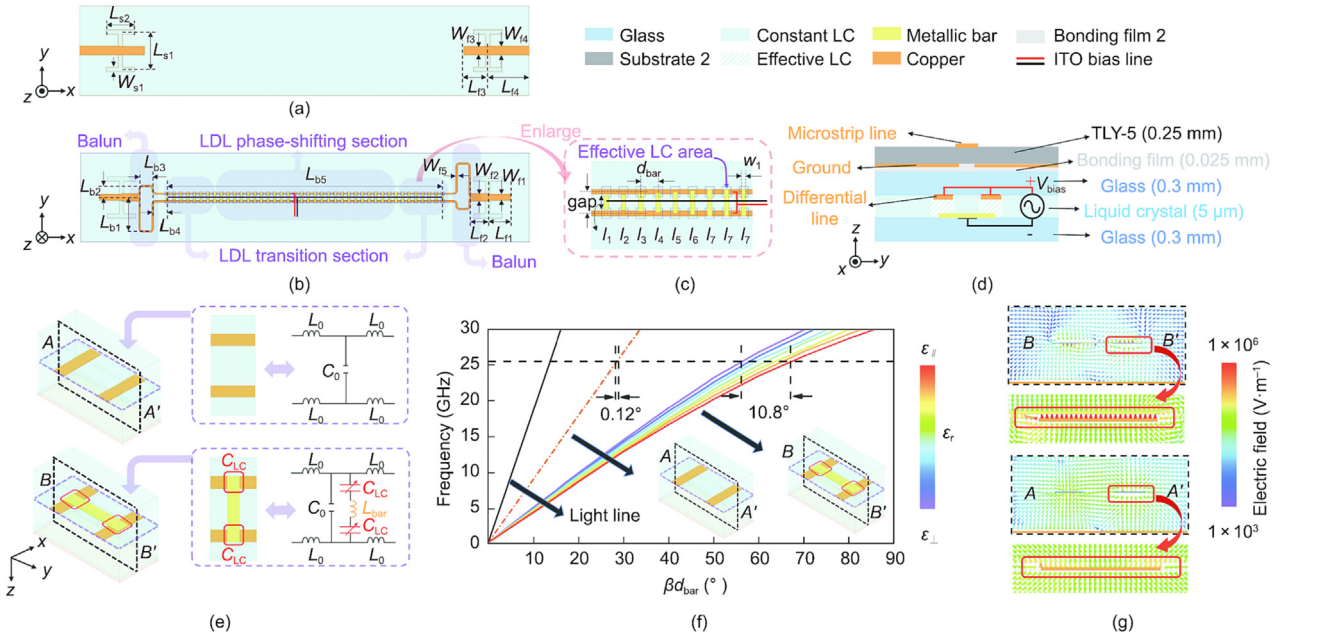

Fig. 2. (a) Top view, (b) bottom view, (c) enlarged view, and (d) side view of an LCPS. The ground layer is set to be transparent in the top and bottom view. The geometrical dimensions in millimeters are as follows: L_{f1} = 1.5, L_{f2} = 1.3, L_{f3} = 1.6, L_{f4} = 2.8, W_{f1} = 0.4, W_{f2} = 0.5, W_{f3} = 0.55, W_{f4} = 0.6, W_{f5} = 0.12, L_{s1} = 2.5, L_{s2} = 1.9, W_{s1} = 0.3, L_{b1} = 2.3, L_{b2} = 0.8, L_{b3} = 0.9, L_{b4} = 0.94, L_{b5} = 18.5, d_{bar} = 0.45, gap = 0.52, w_1 = 0.12, l_1 = 0.33, l_2 = 0.37, l_3 = 0.42, l_4 = 0.47, l_5 = 0.52, l_6 = 0.57, and l_7 = 0.63. The substrates are TLY-5 (ε_r = 2.2, tanδ = 0.0009), glass ($\varepsilon_r \approx$ 4.9, tanδ < 0.01), and bonding film 2 ($\varepsilon_r \approx$ 2.6, tan$\delta \approx$ 0.004). (e–g) Comparisons between the differential line LCPS unit cell without and with the metallic bar loading, including the (e) equivalent circuit, (f) dispersion curves with different values of ε_r, and (g) vectorial electric field distributions. C_0: parallel capacitor; L_0: series inductor; L_{bar}: extra shunt inductor; C_{LC}: two series-connected shunt capacitors; β: phase constant; d_{bar}: LDL cell periodicity; ε_r: dielectric constant of the substrate; tanδ: the loss tangent values.

2.1.2. Simulated and measured results of the LCPSs

In order to verify the performance of the designed LCPSs, a number of prototypes were fabricated and measured. The bottom view and details of an LCPS are displayed in Fig. 3(a). First, the top PCBs and the bottom LDL located on the two glass substrates were manufactured individually. The LCs were filled in between the two glass panels whose separation distance was controlled by glue spacers at the periphery of the glass panels. Then, the two parts were bonded together. Two southwest end-launch connectors were installed at the two microstrip line ports for testing. In order to adjust the permittivity of the LC material, 300 Hz square-wave pulses were applied to the LCPS through a flexible printed circuit. The peak-to-peak value of the bias voltage (V_{bias}) was set within the range of [V_{min}, V_{max}], where V_{min} and V_{max}, defined as the minimum and maximum value of V_{bias}, are set to be 0 V and 23.5 V in our design.

The simulated and measured scattering parameters of the LCPS, which are reported in Figs. 3(b) and (c), show good agreement. The different states of the LCs were realized by changing the permittivity of the LC material in full-wave simulations and by applying different bias voltages in the experiments. The measured reflection coefficient indicates that the proposed LCPS achieves a good impedance match from 24 to 27 GHz with port reflection ($|S_{11}|$) < −15 dB. Both the simulated and measured transmission phases of the LCPS are normalized to align with the case of LCs in the initial state—that is, an unbiased state (V_{bias} = 0 V), at 25.5 GHz. The relationships between the transmission phase and the bias voltage resemble smooth inverted S-shaped curves at all different frequency points from 24.5 to 26.5 GHz. According to the simulations and measurements, the LCPS achieves maximum phase shifts ($\Delta\Phi_{max}$) of about 366° and 390°, and maximum insertion losses (IL_{max}) of around 4 and 5 dB at 25.5 GHz, respectively. The fluctuation of the measured insertion loss is less than 1.3 dB across the frequency band from 24.5 to 26.5 GHz and less than 0.57 dB among different states of the LC material.

To further evaluate the performance of the LCPS, the widely used FoM, which is defined as the ratio of the maximum phase shift to the highest IL [43], was employed:

$$\mathrm{FoM} = \frac{\Delta\Phi_{max}}{IL_{max}} \quad (1)$$

The simulated and measured FoMs of the demonstrated LCPS were found to be 91.7 and 78.3°·dB^{-1}, respectively. A comparison between this LCPS and other previously reported LCPSs operating at frequencies higher than 10 GHz is provided in Table 1 [13,18–20,31,33,35]. It can be seen that the LCPS based on a loaded differential line structure has the highest FoM, while possessing a relatively small footprint and low fabrication complexity. The experimentally achieved full-360° phase coverage of the LCPS, along with its low and stable insertion loss, makes it highly useful for realizing LCPAs with good beam-scanning capabilities.

2.2. Design of the CP element

The configuration of the radiating element of the LCPA is depicted in Fig. 4(a). It contains four substrates and four metallic layers. Substrate 1 and substrate 2 are made of Taconic TLY-5 with a thickness of 0.51 mm and 0.25 mm, respectively, between which is a 0.1 mm-thick bonding film made of Rogers RO4450F. Substrate 3 and substrate 4 are glass, both with a thickness of 0.3 mm. Glue is used on the outer edges of the two glass panels, forming a container with a thickness of 5 μm filled by a homogeneous layer of LCs. Between the top PCBs and the glass panels is a 0.1 mm-thick bonding film. Stacked rectangular patches with a pair of diagonal truncations are employed as the CP radiators, which are printed on the top layers of substrate 1 and substrate 2. The solid metallic layer on the bottom layer of substrate 2 serves as the ground plane of the array elements, where an I-shaped slot is etched out for electromagnetic excitation. On the bottom layer of substrate 3, an embedded microstrip line is used to feed the patches. It should

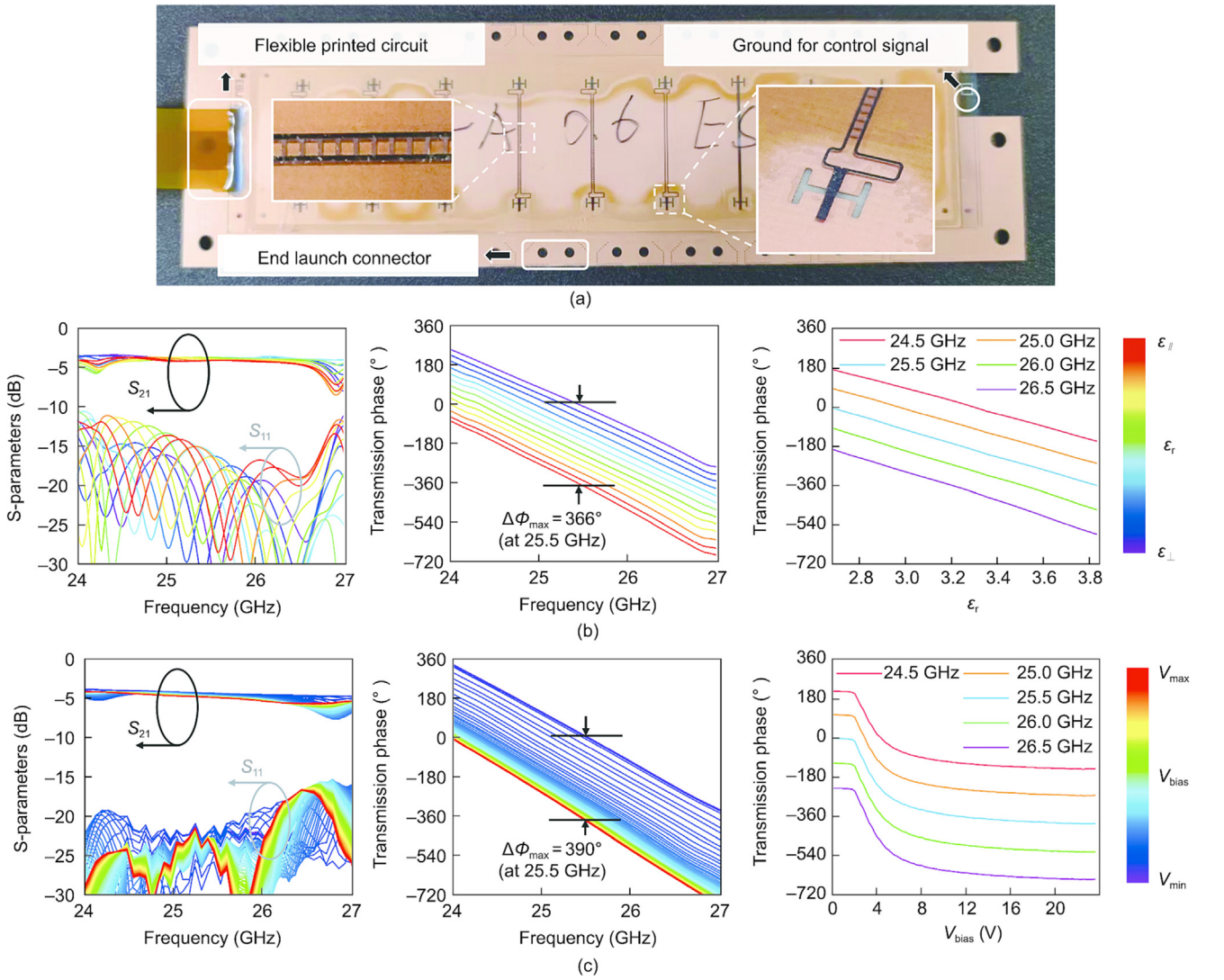

Fig. 3. (a) Photographs of the fabricated LCPS prototypes. The insets show enlarged views of the loaded differential line and balun of the LCPSs. (b) Simulated and (c) measured results of the *S*-parameter magnitudes and transmission phase as a function of frequency, LC permittivity (ε_r), and bias voltage. $\Delta\Phi_{max}$: maximum phase shifts; V_{min}: the minimum value of V_{bias}; V_{max}: the maximum value of V_{bias}; S_{21}: the vertically polarized complex transmission coefficients between the LCPA and probe.

Table 1
A performance comparison of LCPSs.

Structure	f_0 (GHz)	$\Delta\Phi_{max}$ (°)	FoM (°·dB^{-1})	Size ($\lambda_0 \times \lambda_0 \times \lambda_0$)	Ref
IMSL	12.5	146.0	54.3	1.04 × 0.55 × 0.45	[33]
IMSL	17.5	—	62.5	0.65 × 0.65 × 0.09	[13]
CPW	20.0	90.0	60.0	—	[18]
IMSL	28.4	475.0	54.0	1.15 × 0.47 × 0.16	[35]
IMSL	35.0	270.0	38.5	—	[31]
IMSL	37.0	202.0	26.0	0.96 × 0.95 × 0.07	[19]
LC-NaM[a]	56.0	116.0	70.0	0.67 × 0.34 × 0.14	[20]
LDL	25.5	390.0	78.3	2.35 × 0.51 × 0.07	This work

CPW: coplanar waveguide; f_0: the center frequency of operational band; λ_0: the wavelength at the center frequency.
[a] Substrates based on LCs and a metallic nanowire-filled porous alumina membrane (NaM).

be noted that the LCPS is also placed on this layer, in between the two glass panels. More detailed dimension information is presented in the top and bottom views, as shown in Figs. 4(b) and (c).

The simulated results of the reflection coefficient, axial ratio (AR), and gain of the LC-based CP element are illustrated in Fig. 4(d). The element achieves a good impedance match, with $|S_{11}| < -14$ dB from 24 to 27 GHz. At frequencies ranging from 24.95 to 26.06 GHz, the element radiates a right-handed circularly polarized (RHCP) wave with an AR < 3 dB. The maximum gain value reaches 4.86 dBic with a gain variation of less than 0.5 dB.

2.3. Integrated configuration and fabrication of the LCPA

In order to combine the channels of the CP elements and LCPSs into an integrated array, an *N*-way power divider was designed. The integrated configuration of the LCPA, with an overall footprint

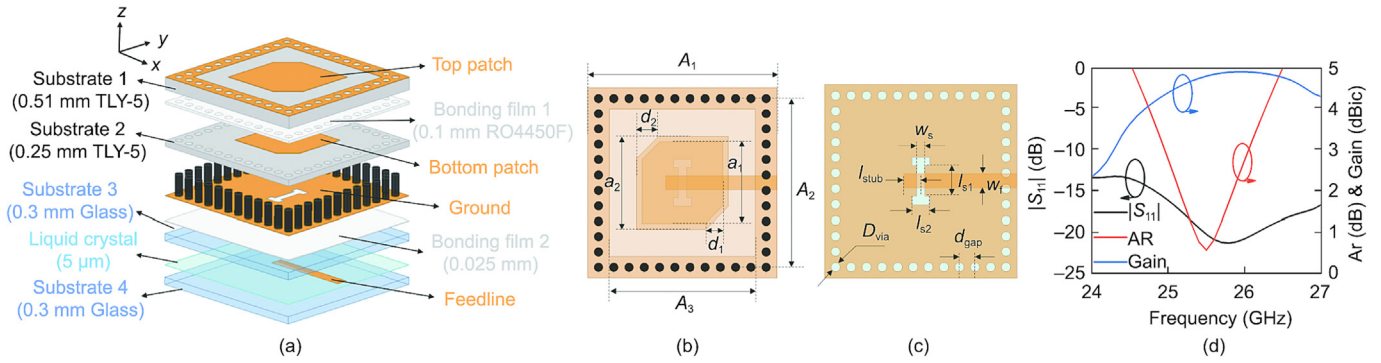

Fig. 4. (a) 3D view, (b) top view, (c) bottom view, and (d) simulated $|S_{11}|$, axial ratio (AR), and gain of the CP element of the LCPA. The geometrical dimensions in millimeters are A_1 = 6.7, A_2 = 6, A_3 = 5.2, a_1 = 2.9, a_2 = 3.3, d_1 = 0.62, d_2 = 0.8, w_s = 0.3, l_{s1} = 1.07, l_{s2} = 0.64, l_{stub} = 0.6, w_f = 0.5, D_{via} = 0.32, and d_{gap} = 0.55. The substrates are TLY-5 (ε_r = 2.2, tanδ = 0.0009), Rogers RO4450F (ε_r = 3.52, tanδ = 0.004), glass ($\varepsilon_r \approx$ 4.9, tanδ < 0.01), bonding film 2 ($\varepsilon_r \approx$ 2.6, tan$\delta \approx$ 0.004), and homogeneous liquid crystal (ε_r = 2.66, tanδ = 0.015).

of 195 mm × 91.7 mm and a thickness of 1.76 mm, is shown in Fig. 5(a); it includes a 1–16 stripline power divider, 16 LCPSs, 16 CP radiating elements, and two dummy elements. To facilitate the connection of the control board, the substrate is slightly extended on both the left and right sides. Moreover, a stepped board process is introduced at the input port for converting the stripline into a microstrip line that can be more easily connected to a southwest end-launch connector. The characteristic impedance of the input microstrip line is set to be 50 Ω, with a width of 0.65 mm.

The detailed geometry of different portions of the stripline power divider with a corporate feeding structure is displayed in Fig. 5(b). There are four stages of cascaded "T"-shaped 1–2 power dividers for realizing an equal power division between the 16 output ports. At the input port, three sections of quarter-wave stripline are employed to improve the impedance match. As shown

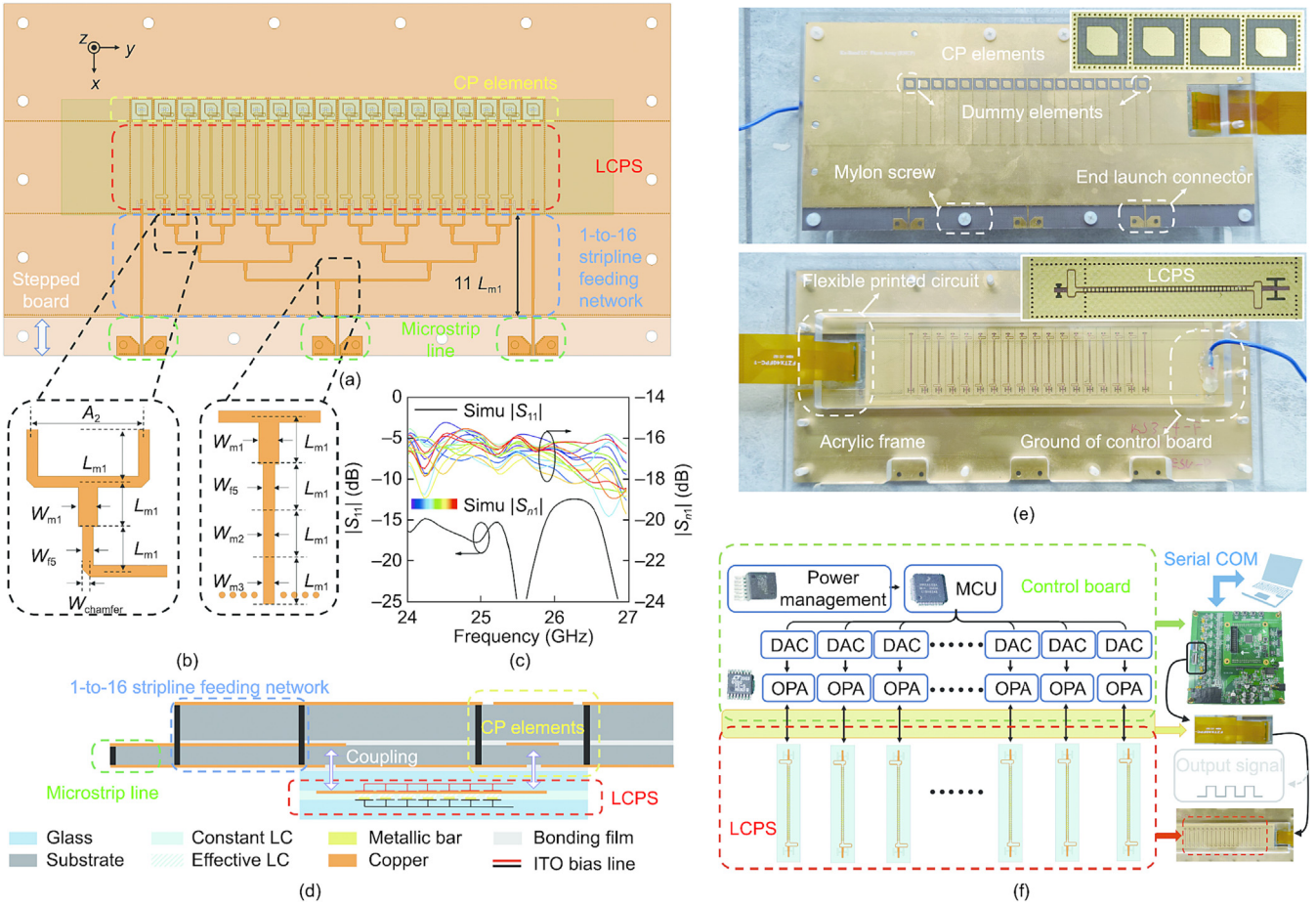

Fig. 5. (a) Schematic of the proposed LCPA. (b) Enlarged view and (c) simulated scattering parameters of the entire feeding network, including the 1–16 power divider and LCPSs when the beam scanning angle θ_{scan} = 0°. (d) Side view of the LCPA. The geometrical dimensions are L_{m1} = 2.4, W_{f5} = 0.6, W_{m1} = 1.05, W_{m2} = 0.57, W_{m3} = 0.55, and $W_{chamfer}$ = 0.42, all in millimeters. (e) Top view and bottom view of the fabricated LCPA. The insets show enlarged views of the CP elements and LCPS. (f) Configuration and hardware implementation of the control board. Simu: simulated; MCU: microcontroller unit; DAC: digital-to-analog converter; OPA: operational amplifier.

in Fig. 5(c), the 1–16 power divider, together with the phase shifters, possesses a return loss of greater than 12.5 dB within the frequency band from 24 to 27 GHz. The overall insertion loss for the case in which the beam scans to broadside—that is, the beam scanning angle θ_{scan} equals to 0°—is 4.55 dB at 25.5 GHz, which can still be maintained within 4.38 to 4.64 dB when the beam scans from −40° to +40°.

Fig. 5(d) illustrates the laminated structure of the proposed LCPA, where the upper PCBs and the lower glass panels are connected by means of a bonding film without any direct metallic connection. Compared with the conventional LC filling method, in which a cavity must be milled in the substrate for LC filling [31], the employed structure allows for the separated fabrication of the CP elements and glass-based LCPSs, thereby improving the manufacturing efficiency and uniformity of the LC filling. The integrated 16-element LCPA was fabricated and fixed on an acrylic frame using nylon screws (Fig. 5(e)). The enlarged view at the top right of the figure illustrates the CP radiation elements and that at the bottom right illustrates the LCPS. A flexible printed circuit is used to connect the ITO bias lines for all the channels to the control board.

2.4. Design and implementation of the control board

After the design and fabrication of the LCPA, another critical part of the sub-system is the control circuit, which is responsible for applying the correct bias voltage to each channel. The control board includes a microcontroller unit (MCU) and 16 operational amplifiers (OPAs), which provide bias voltages in the form of square pulses for the 16 channels individually (Fig. 5(f)). The power management of the control board includes a source module and a low dropout linear chip. For each channel of the LCPA, the top bias lines are connected in parallel to the control board through the flexible printed circuit. The bias lines on the bottom, however, are combined together for all the channels and connected to the ground.

In terms of functionality, the control board is designed to generate multiple square waves with adjustable voltages of alternating current (AC) source. First, the original digital signals output from the MCU is transformed into analog signals by the built-in digital-to-analog converters (DACs). The appropriate voltage of the analog signals is then obtained using an OPA. Finally, a 300 Hz square wave with a bias voltage in the range of 0–23.5 V is generated by the control circuit and applied to the ITO electrodes of the LCPS via the flexible printed circuit. By establishing serial communication between the MCU and the PC, the state of each LCPA channel can be individually controlled by applying the targeted bias voltage. With the help of the control board, the automatic in-array calibration and phase assignment of the LCPA can be further implemented, as will be described in the next section.

3. In-array calibration of the LCPA

In order to achieve the desired beam-scanning functionality, calibration is indispensable for phased arrays with a large number of channels. Unlike conventional phased arrays based on digital phase shifters, for LCPAs, the relationship between the phase shifts and bias voltage is unknown and differs from channel to channel. Hence, the phase–voltage relationship of each individual channel, including the initial phase and line shape of the phase shift-voltage curve, must be extracted in the array environment. To this end, an SEM is proposed and implemented to achieve automatic LCPA calibration by utilizing the ergodic states of LC molecule deflection without relying on any prior knowledge.

3.1. Theory of the state ergodic method

For the OTA in-array calibration of a conventional phased array, only the channel under test is turned on (i.e., is radiating), while all the other channels are turned off (i.e., are not radiating) [44]. However, for the LCPAs, all the channels are turned on simultaneously. Considering an LCPA of N channels calibrated by a scanning near-field probe placed in front of the array at a distance of about $0.5\lambda_0$ to $1.5\lambda_0$ (Fig. 6(a)), a multipath transmission model can be used to describe the waves received by the probe. As such, the received signal is a superposition of the waves radiated from all the channels, as follows:

$$\boldsymbol{S}^{a}_{i,k} = \boldsymbol{S}^{c}_{i,k,k} + \sum_{j=1,j\neq k}^{N} \boldsymbol{S}^{c}_{1,j,k} \tag{2}$$

where $\boldsymbol{S}^{a}_{i,k}$ denotes the total signal received by the probe when channel k is being calibrated and applied with a bias voltage of V_i, while the contribution of the fields radiated by each single channel j with a bias voltage of V_i is $\boldsymbol{S}^{c}_{i,j,k}$. Since different bias voltages are applied to each channel when it is under calibration, the voltage set can be denoted as $\boldsymbol{V} = \{V_1, V_2, \ldots, V_i, \ldots, V_n\}$, where the total number of ergodic states is M and $V_i \in [V_{min}, V_{max}]$. Graphically, $\boldsymbol{S}^{a}_{i,k}$ and $\boldsymbol{S}^{c}_{i,j,k}$ can be described as vectors due to their complex nature. Hence, the purpose becomes to obtain the quantity $\boldsymbol{S}^{c}_{i,k,k}$ for $i = 1, 2, \ldots, M$, and $k = 1, 2, \ldots, N$, which can be used to retrieve the distinct phase–voltage curves of all the channels.

When extracting $\boldsymbol{S}^{c}_{i,k,k}$ of channel k, the bias voltages for all the other channels are set to be unchanged, such as at 0 V, which ensures that the influence of the radiated fields from the other channels are kept the same. Under such circumstances, the summation of the fields radiated from all the other channels except for channel k, namely $\sum_{j=1,j\neq k}^{N} \boldsymbol{S}^{c}_{1,j,k}$, can be regarded as nearly a constant, which is defined as the environment signal $\boldsymbol{S}^{e}_{k}$. Thus, any complex signal $\boldsymbol{S}^{a}_{i,k}$ directly measured by the probe can be represented by a vectorial superposition of $\boldsymbol{S}^{e}_{k}$ and $\boldsymbol{S}^{c}_{i,k,k}$ in the complex plane, as shown in Fig. 6(b). The required $\boldsymbol{S}^{c}_{i,k,k}$ corresponding to channel k alone under a bias voltage V_i can be described as follows:

$$\boldsymbol{S}^{c}_{i,k,k} = \boldsymbol{S}^{a}_{i,k} - \boldsymbol{S}^{e}_{k} \tag{3}$$

With a nearly unchanged environment signal $\boldsymbol{S}^{e}_{k}$, according to our experimental observations, the endpoint trajectory of the vector $\boldsymbol{S}^{a}_{i,k}$ resembles a quasi-ellipse in the complex plane as V_i traverses from V_{min} to V_{max}. As shown in Fig. 6(c), the shape of the ellipse is determined by the response $\boldsymbol{S}^{c}_{i,k,k}$ of channel k, including both the amplitudes and phases of the radiated field with different bias voltages, while the center of the ellipse is determined by the environment vector $\boldsymbol{S}^{e}_{k}$. Because the phase shift of each channel is not linearly proportional to the bias voltage, as revealed by the measured results in Section 2.1, the endpoints of $\boldsymbol{S}^{a}_{i,k}$ would not be uniformly distributed on the ellipse. It should also be noted that, in practice, the endpoints of $\boldsymbol{S}^{a}_{i,k}$ may not be able to trace out a complete ellipse under circumstances when the phase-shifting range of the channel is smaller than 360°.

Since only the complex value of $\boldsymbol{S}^{a}_{i,k}$ can be directly recorded in an experiment, it becomes important to extract the near-constant environment vector $\boldsymbol{S}^{e}_{k}$ that is uncorrelated to the bias voltage V_i applied to the channel under calibration. Mathematically, the problem to be solved is to find the coordinates of the center of the quasi-elliptical trace on the complex plane. To this end, as illustrated in Fig. 6(d), an ellipse fitting algorithm is employed with the fitted ellipse function written as follows:

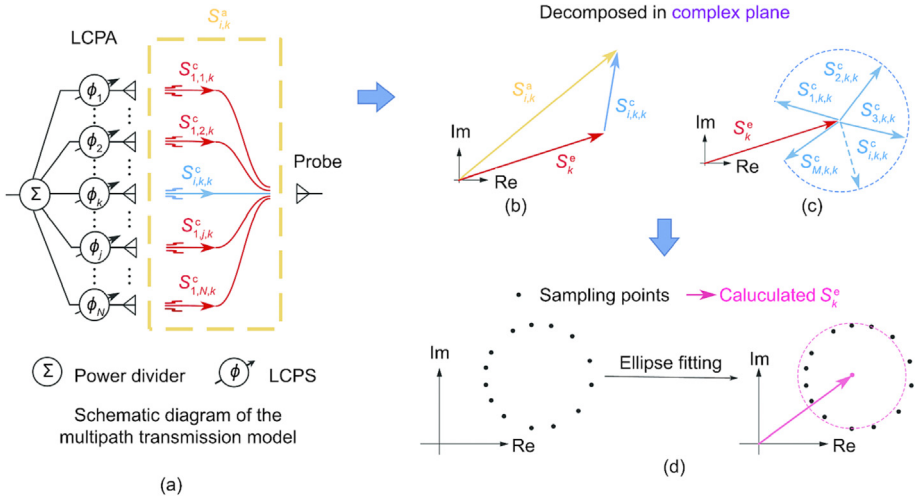

Fig. 6. (a) Schematic diagram of the multipath transmission model. (b) Vectorial relationship between $\boldsymbol{S}^{c}_{i,k,k}$, $\boldsymbol{S}^{a}_{i,k}$, and $\boldsymbol{S}^{e}_{k}$. (c) Vectorial diagram of $\boldsymbol{S}^{c}_{i,k,k}$ and $\boldsymbol{S}^{e}_{k}$ while the bias voltage of channel k is traversing different values. (d) Schematic diagram of environment vector extraction using an ellipse fitting algorithm. Im: the imaginary axis of the complex plane; Re: the imaginary axis of the complex plane.

$$\left(\frac{Re(\boldsymbol{S}^{a}_{i,k})-Re(\boldsymbol{S}^{e}_{k})}{a}\right)^{2}+\left(\frac{Im(\boldsymbol{S}^{a}_{i,k})-Im(\boldsymbol{S}^{e}_{k})}{b}\right)^{2}=1 \tag{4}$$

where, Re(·) and Im(·) represent the real part and imaginary part of the complex signal, respectively, a and b are the major and minor axes of the ellipse, respectively. Hence, the coordinates of the fitted ellipse center—that is, the environment vector $\boldsymbol{S}^{e}_{k}$—can be obtained by using an optimization algorithm for the least squares fitting of the ellipse [45], which can make full use of the responses of each channel under calibration in all different LC states. Importantly, such a method could be effective for LCPA channels with almost any kind of phase-shift coverage and phase–voltage relationships.

3.2. The OTA in-array calibration setup and procedure

In order to implement the proposed SEM for the phase–voltage curve extraction of the in-array channels of the LCPA, an automatic calibration system is implemented (Fig. 7(a)). The system includes an LCPA along with the control board, a dual-linearly polarized open-waveguide probe, a vector network analyzer, a robotic arm with a precise displacement machine, and a PC for controlling the above devices. As shown in Fig. 7(b), port 1 of the vector network analyzer is connected to the input port of the LCPA, while port 2 and port 3 are connected to the two input ports of the open-waveguide probe for receiving the two orthogonal linearly polarized wave components emitted from the LCPA channels. The values of S_{21} and S_{31} represent the vertically polarized (VP) and horizontally polarized (HP) complex transmission coefficients between the LCPA and probe, respectively. The probe is fixed on the robotic arm, which can be moved in the horizontal direction in front of the LCPA elements. The robotic arm, control board, and vector network analyzer (VNA) are all connected to the PC through serial communication or socket communication, for realizing the automatic procedures of the moving probe, applying bias voltages, and recording data, respectively.

A flowchart of the automatic OTA in-array calibration is shown in Fig. 7(c). First, the dual-port open-waveguide probe is placed in front of the radiating element of the channel k with k = 1. Second, different bias voltages V_i are applied to the channel k of the LCPA through the control board, and the two corresponding linearly polarized transmission coefficients, $\boldsymbol{S}^{a,HP}_{i,k}$ and $\boldsymbol{S}^{a,VP}_{i,k}$, are recorded, from which the RHCP transmission coefficient, that is, $\boldsymbol{S}^{a,RHCP}_{i,k}$, can be obtained. This step iterates until the data for all different bias voltages of V_i ranging from 0 to 23.5 V, with a step of 0.1 V, are recorded. Third, based on the calculated $\boldsymbol{S}^{a,RHCP}_{i,k}$, the RHCP environment vector of channel k, that is, $\boldsymbol{S}^{e,RHCP}_{i,k}$, can be extracted by the

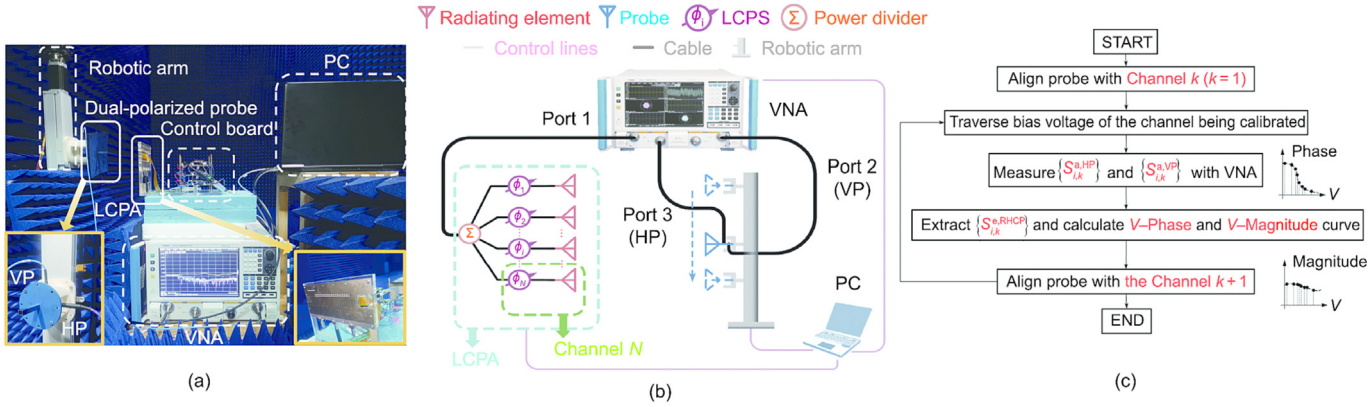

Fig. 7. (a) Photographs of the LCPA being calibrated using a dual-polarized probe in the near field. (b) Schematic of the OTA automatic calibration. (c) Flowchart for the automatic calibration of an RHCP LCPA with N channels. VP: vertically polarized; HP: horizontally polarized; VNA: vector network analyzer.

ellipse fitting algorithm. Furthermore, the phase–voltage curves can be calculated utilizing Eq. (3). Then, the probe moves to the next channel to calibrate channel ($k + 1$). The abovementioned iterative procedure continues until the calibration for all the channels is completed; namely, the phase–voltage dataset with a size of $N \times M$ is recorded at every frequency point within the required frequency band.

3.3. Phase–voltage curve extraction of the LCPA channels

Based on the proposed SEM calibration strategy and the automatic calibration procedure, the phase–voltage curves of the 16 channels of the LCPA at 24.5, 25.0, 25.5, 26.0, and 26.5 GHz were obtained, as shown in Fig. 8(a). To facilitate comparison, all the curves are normalized to the initial phase, with V_{bias} = 0 V at each frequency. It can be seen that the transmission phases of the LCPA channels as a function of the bias voltage all share a line shape similar to that of the LCPS illustrated in Section 2—that is, an inverted S-shaped curve—which corroborates the measurement results reported previously in the literature [46,47]. From 24.5 to 26.5 GHz, the averaged maximum phase shift $\Delta\Phi_{max}$ among all 16 channels is 258°, 286.6°, 288.7°, 306.1°, and 315.2°, respectively, which covers the majority of a full cycle. The difference in $\Delta\Phi_{max}$ among the 16 channels at the five frequency points is about 50.4°, 41.9°, 43.4°, 47.9°, and 27.8°, respectively. Such a difference in phase coverage among the channels mainly comes from the nonuniform thickness of the LC layer, whose thickness can be controlled within a fabrication error of less than 10%. More consistent responses from the LCPA channels can be expected with further improvement of the fabrication accuracy. The normalized transmission magnitudes as a function of the bias voltage for the 16 channels at different frequencies are presented in Fig. 8(b), exhibiting a variation of less than 1.5 dB under different bias voltages from 24.5 to 25.5 GHz. At higher frequencies, the fluctuation slightly increases to around 2 dB due to the existence of a resonance.

In order to further evaluate the static characteristics of each channel in an unbiased state with V_{bias} = 0 V, the extracted initial phases and normalized transmission magnitudes of the 16 channels at different frequencies are reported in Figs. 8(c) and (d),

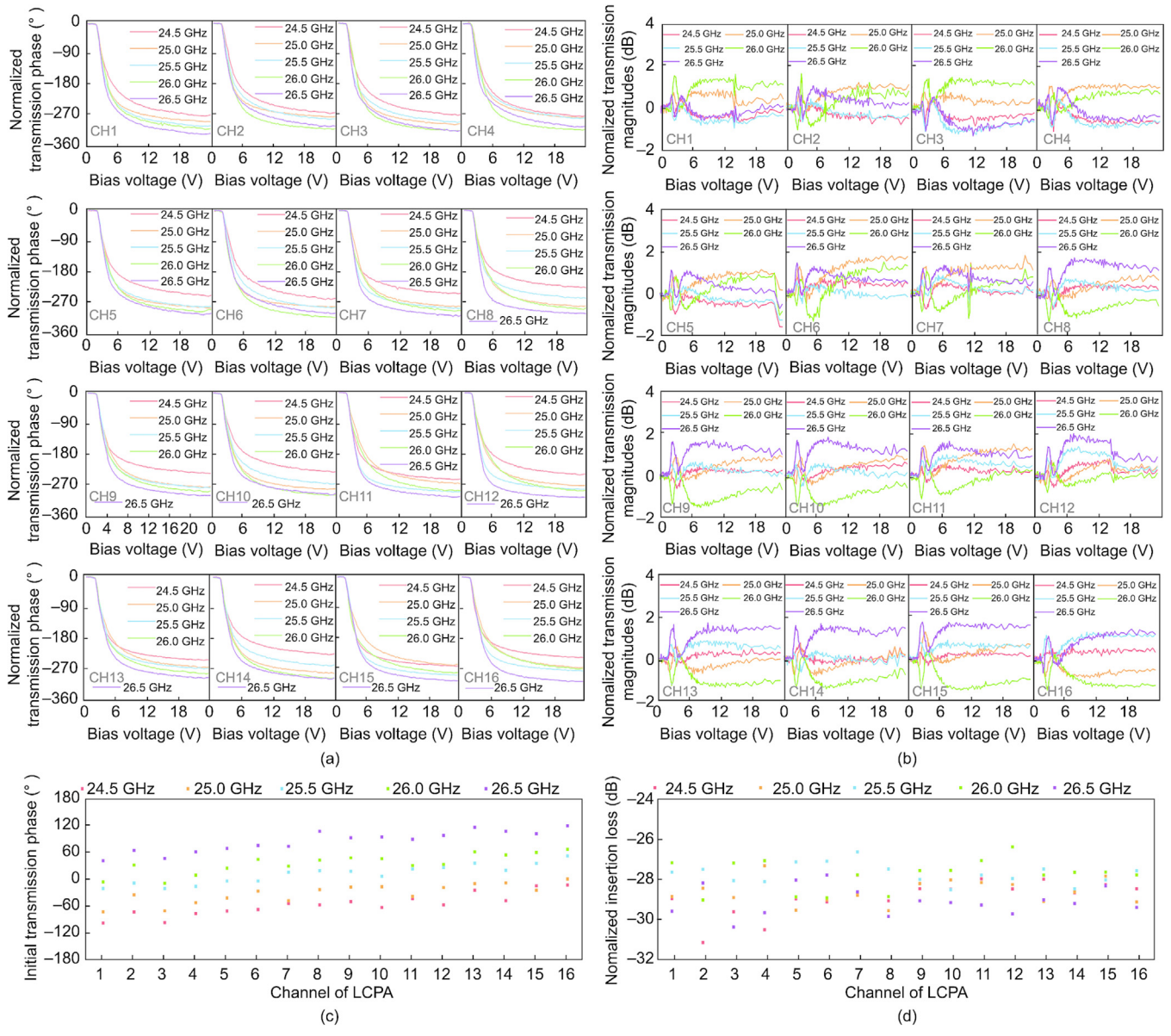

Fig. 8. Extracted normalized (a) transmission phases and (b) magnitudes of the 16 LCPA channels as a function of the bias voltage at 24.5, 25.0, 25.5, 26.0, and 26.5 GHz. (c) Initial phases and (d) transmission magnitudes of the 16 LCPA channels with V_{bias} = 0 V. CH: channel.

respectively. It can be seen that the initial phases of the 16 channels quasi-monotonically increase as a function of the channel number, with a variation of about 60°. The normalized transmission magnitudes among different channels also show a small fluctuation of less than 2 dB at the central frequency of 25.5 GHz and of about 3 dB at the lower or higher frequency ends.

In summary, response differences can be observed among all the LCPA channels in terms of both transmission magnitude and phase. This phenomenon is mainly attributed to the non-uniform thickness of the LC and the deposited copper layers, which is difficult to completely eliminate due to the extreme thinness of the LC layer. Hence, the proposed automatic OTA calibration method, which can effectively extract the characteristics of each individual channel in the LCPA, becomes particularly important. The transmission phase difference can be effectively extracted by the SEM and separately compensated for, thereby ensuring the accuracy of far-field beam scanning. The fluctuation in the transmission magnitudes is less than 3 dB; that is, the amplitude variation in the radiated fields among all the elements is no greater than 1.5 dB and thus will only have a minor influence on the steerable beams of the LCPA. It should be mentioned that the response of the LCPA channels remains stable even after thousands of switching cycles of repeatedly changing the bias voltage.

4. Experimental results

4.1. Calculation of bias voltage distribution

Based on the extracted phase–voltage curves of each channel of the LCPA, the bias voltage distributions of the proposed linear LCPA for achieving steerable directive beams can be obtained. For a beam pointing at the direction θ_{scan}, the excitation phase φ_j required for element E_j can be described as follows:

$$\varphi_j = \varphi_0 + (j-1)k_0 d \sin\theta_{\text{scan}} \tag{5}$$

where d is the spacing between the array elements, φ_0 is a redundant reference phase that refers to the initial phase of the first element E_1 in the LCPA. According to the tunability principle of the LCPA, φ_j can be achieved by applying the bias voltage V_j according to the extracted relationship between the phase and voltage for channel j, as described by $\varphi_j = f_j(V_j)$. The schematic diagram for the phase assignment is shown in Fig. 9(a), where the phase–voltage curves are represented by black lines and the LC states of each channel are marked as yellow dots. The required bias voltage V_j can be obtained by mapping the corresponding excited phase φ_j to the phase–voltage curve; that is, $V_j = f_j^{-1}(\varphi_j)$. It should be noted that the desired phase distribution for pointing the beam at θ_{scan} is not unique. In other words, the reference phase φ_0 is an optimizable variable. When testing the far-field pattern of the LCPA with beams steered at different θ_{scan}, the value of φ_0 is tuned to obtain beams with better performance.

Since the operational bandwidth of the LCPA is relatively narrow, only the phase–voltage curves of all the channels at 25.5 GHz were utilized when calculating the desirable bias voltages for different scanned beams. For verification, a total of 13 pencil beams scanning from −60° to +60° were generated with a step of 10°; their bias voltages were calculated and are listed in Table 2.

4.2. Simulated and measured results of the LCPA

In order to verify the proposed LCPA, a prototype was measured in an anechoic far-field chamber with its RHCP beam steering from −60° to +60° and with a step of 10°, by applying appropriate bias voltage sets to the LCPA (Fig. 9(b)). The simulated and measured $|S_{11}|$ of the LCPA with different beam directions are displayed in Fig. 9(c). It can be observed that the reflection coefficient remains below −10 dB for all cases from 23.6 to 28 GHz for the simulated results and from 23.5 to 28 GHz for the measured results. The variation in the measured $|S_{11}|$ due to different bias voltage sets being applied to the LCPA is less than 2 dB, implying that the LCPA can maintain a stable and well-matched input impedance.

The simulated and measured far-field RHCP gain patterns and AR patterns of the LCPA at 25.50, 25.75, and 26.00 GHz are reported in Fig. 10 for cases with different beam-scanning angles. It should be noted that the simulated patterns were obtained based on array synthesis theory [48] and the cascading method of multi-port networks [49], where the vectorial radiated fields and S-parameters of the array elements, LCPSs, and feeding network must be separately simulated and extracted. It can be observed that the simulated and measured patterns agree well with each other at all three frequencies in terms of the beam pointing angle and beam shape. When the scanning angle is gradually increased from broadside to ±60°, the half-power beamwidth of the main beam is broadened from 6° to 8° with a scanning loss of less than 3 dB. At 25.5 GHz, the maximum sidelobe levels (SLLs) of all the patterns are kept below −10 dB. No significant beam shape distortion or abnormally high sidelobes occur, even for beams with a large scanning angle. The measured AR pattern also matches well with the simulated results, indicating that scanning CP beams with AR < 3 dB can be obtained

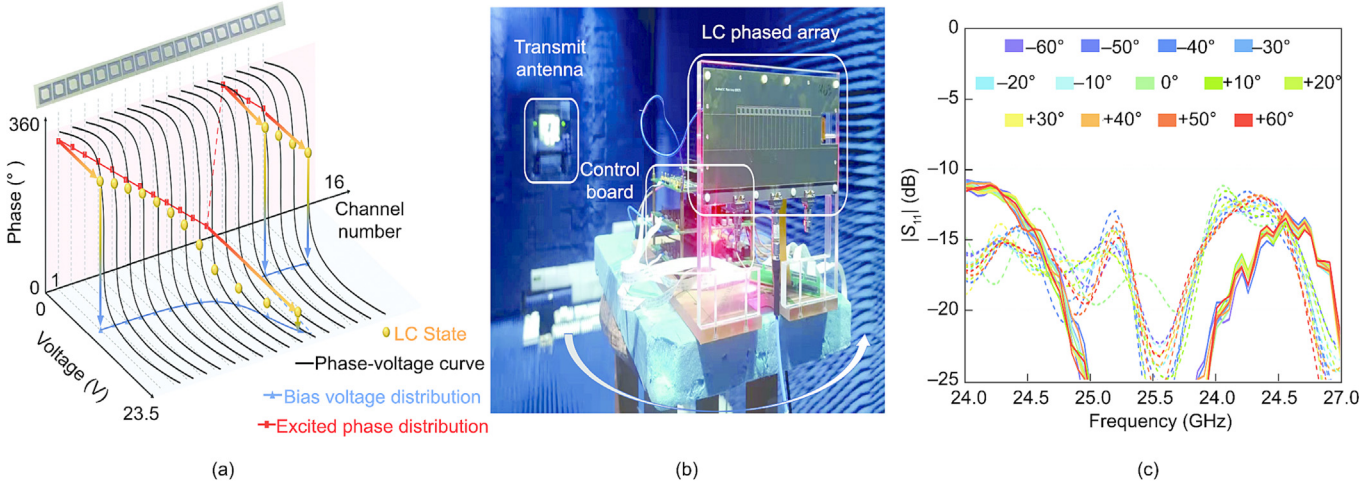

Fig. 9. (a) Schematic diagram of the voltage configuration for 1 × 16 LCPA. (b) A photograph of the LCPA prototype being tested in an anechoic far-field chamber. (c) The simulated and measured $|S_{11}|$ of the LCPA as a function of frequency when the RHCP beam scans from −60° to +60°.

Table 2
Bias voltage configurations for 16 channels under different beam directions (calculated at 25.5 GHz).

Beam direction	Bias voltages (V)															
	CH1	CH2	CH3	CH4	CH5	CH6	CH7	CH8	CH9	CH10	CH11	CH12	CH13	CH14	CH15	CH16
−60°	0.7	6.9	2.5	15.0	3.3	1.4	4.4	2.3	8.6	2.8	23.5	3.7	0.1	4.8	2.1	14.0
−50°	4.0	2.6	7.8	3.5	2.1	7.0	3.1	1.2	5.8	2.6	23.5	4.1	2.2	8.4	3.0	0.1
−40°	6.9	3.7	2.2	23.5	4.1	2.6	23.5	5.4	3.1	1.4	6.8	3.2	1.8	8.2	3.5	2.2
−30°	2.3	0.1	5.1	3.6	2.7	0.3	7.4	4.5	3.0	1.9	13.4	4.9	3.1	2.0	23.5	6.4
−20°	0.7	0.1	5.8	4.6	3.6	2.7	2.0	1.2	23.5	5.8	4.1	3.0	2.3	1.4	23.5	8.8
−10°	2.9	2.8	2.4	2.1	1.8	1.4	23.5	23.5	13.0	6.5	5.5	4.5	3.9	3.1	2.6	2.7
0°	4.2	5.7	4.3	5.2	5.4	5.4	5.7	6.9	8.2	7.4	8.2	9.0	13.0	8.8	11.4	18.0
+10°	2.7	3.4	3.6	4.6	6.2	15.6	23.5	1.2	2.0	2.5	2.8	3.3	4.2	4.5	7.2	17.5
+20°	7.9	1.7	2.3	3.0	4.1	6.7	23.5	2.0	2.9	3.6	5.8	20.5	0.1	2.4	2.9	5.0
+30°	5.1	0.1	2.5	3.6	7.3	0.3	2.7	4.5	23.5	1.9	2.9	4.9	23.5	2.0	2.9	6.4
+40°	0.7	3.4	5.6	1.8	3.4	8.2	0.7	3.7	11.2	2.0	3.5	9.4	1.9	3.3	9.6	1.9
+50°	2.6	7.3	0.2	3.5	23.5	2.6	5.2	1.8	3.9	23.5	2.4	5.6	0.1	3.2	14.6	2.5
+60°	12.8	2.9	5.6	2.4	5.1	2.1	4.2	1.2	3.8	23.5	2.9	9.8	2.4	5.3	1.5	4.8

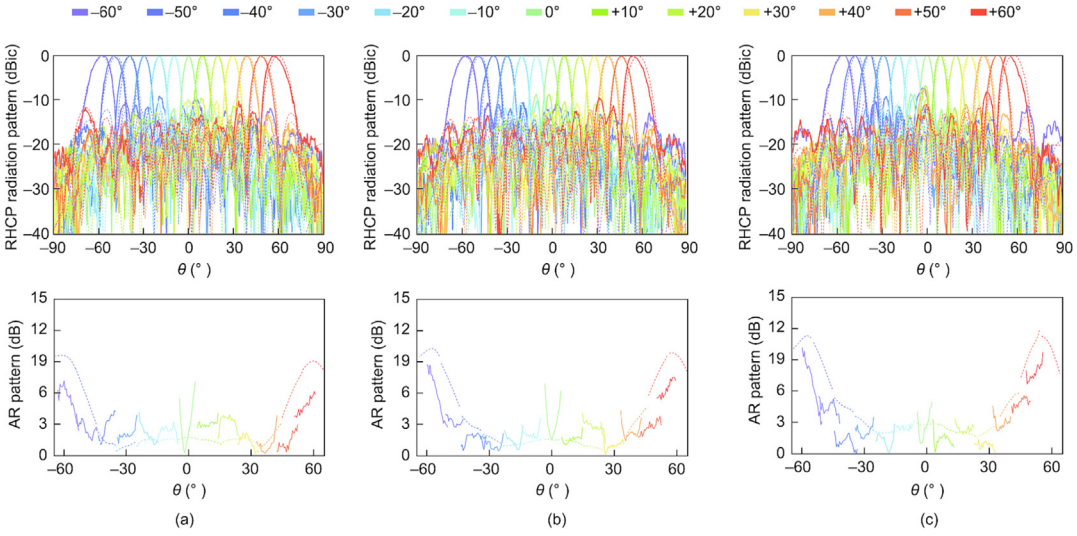

Fig. 10. Simulated (dashed curves) and measured (solid curves) far-field RHCP gain patterns and AR patterns of the LCPA prototype with different beam-scanning angles changing from −60° to +60° at (a) 25.50, (b) 25.75, and (c) 26.00 GHz.

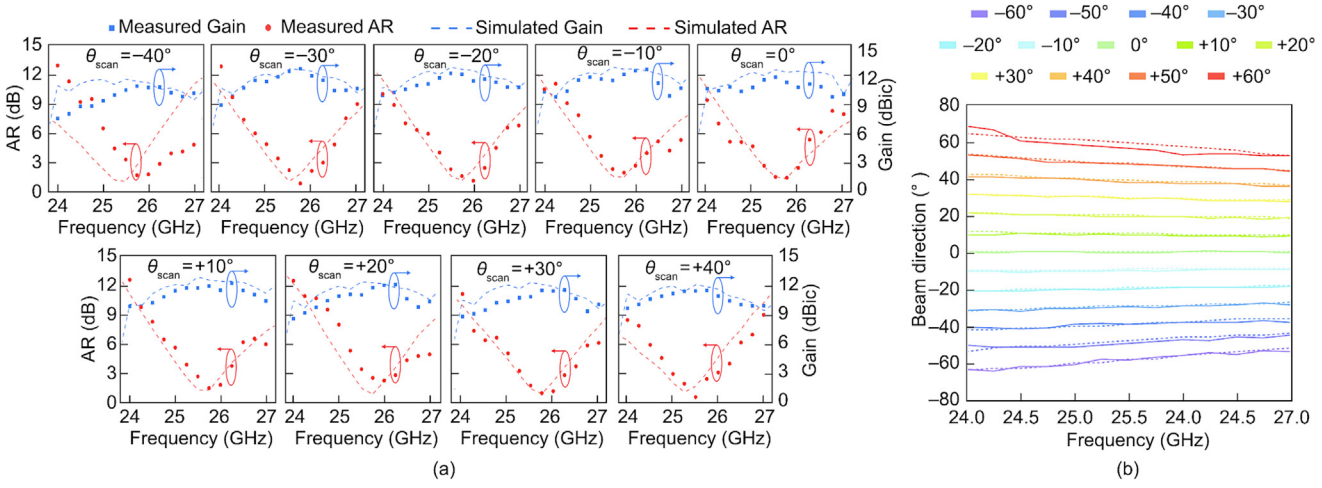

Fig. 11. (a) Simulated and measured gain and AR as a function of the frequency of the LCPA with beam steering from −40° to +40°. (b) Simulated and measured beam direction as a function of the frequency of the LCPA with beam steering from −60° to +60°.

Table 3
A performance comparison of LCPAs.

f_0 (GHz)	Polarization	Antenna type	Impedance Bandwidth (%)	Channel number	Scanning range (°)	SLL (θ_{scan} = 0°) (dB)	SLL (θ_{scan} = max) (dB)	Realized gain (θ_{scan} = 0°)	Realized gain (θ_{scan} = max)	AR BW	LC layer thickness (μm)	Total efficiency (%)	Ref.
17.5	LP	Patch	7.40	4	±25	−6	−4	5.9 dBi	3.9 dBi	—	100	~21.2	[13]
35.0	LP	ME dipole	5.20	4	±22	−9	−3	6.7 dBi	2.8 dBi	—	127	~25.2	[31]
28.0	LP	Parasitic patch	8.30	3	±28	−10	−8	6.0 dBi	5.0 dBi	—	254	—	[32]
12.5	LP	Patch	6.00	4	±16	−9	−8	—	3.0 dBi	—	250	<22.8	[33]
10.0	LP	Dielectric resonator	—	4	±30	−13	−4	4.3 dBi	2.8 dBi	—	100	—	[34]
28.4	LP	Yagi-Uda	20.70	4	±40	−8	−2	4.5 dBi	3.2 dBi	—	20	~8.6	[35]
4.0	LP	Patch subarray	12.60	4	±20	−17	−8	12.9 dBi	—	—	4	~30.5	[36]
25.5	CP	Stacked patch	> 11.70	16	±40 (3 dB AR)	−12	−10	12.5 dBic	10.5 dBic	0.5 GHz	5	~33.9	This work

from −40° to +40° within the band from 25.5 to 26.0 GHz. Both the measured results of the AR and the gain pattern confirm the validity of the proposed OTA in-array calibration method and the correctness of the bias voltage sets for beamforming. The far-field patterns were measured repeatedly under different temperatures of 10 and 30 °C, respectively. The corresponding patterns remained almost unchanged, indicating that the LCPA has a stable radiation performance within normal temperature fluctuation.

The gain and AR curves of the beams steering at directions ranging from −40° to +40° as a function of frequency are displayed in Fig. 11(a). The maximum gain values of the nine beams are about 11.2, 11.8, 12.2, 12.5, and 12.4 dBic at 25.00, 25.25, 25.50, 25.75, and 26.00 GHz, respectively. The 3 dB gain bandwidth covers from 24.25 to 27.00 GHz, corresponding to a relative bandwidth of 8.7%, with a gain fluctuation of less than 2.5 dB for all the beams at all five frequencies. The averaged difference between the simulated and measured gain is about 0.7 dB, which can be attributed to the non-ideal gradient phase excitation due to the imperfect calibration of the channels and the non-uniform amplitude excitation caused by the inherent inconsistencies among different channels. The AR of the generated CP beams is below 3 dB from 25.5 to 26.0 GHz for all nine beams, indicating that the LCPA possesses stable CP radiation as the beam scans from −40° to +40°. When the scanning angle is further increased to ±50° and ±60°, the AR bandwidth of the CP beam becomes narrower and shifts toward lower frequencies. For all the CP beams scanning from −60° to +60°, the AR value remains smaller than 6 dB in the frequency band from 25.2 to 25.6 GHz. The simulated and measured beam directions of the thirteen beams are presented in Fig. 11(b). It can be seen that the beam direction error is less than 3° at 25.5 GHz within a scanning range between −60° and +60°. Within the frequency band from 25.0 to 26.0 GHz, the simulated and measured maximum beam squinting is within ±3° and ±4°, respectively.

A detailed comparison between the proposed LCPA and its previously reported counterparts is provided in Table 3 [13,31–36]. First, compared with existing designs, the proposed LCPA realizes CP radiation characteristics, while the others are linearly polarized. Second, the demonstrated LCPA possesses a wide scanning angle from −40° to +40°. Third, the array contains more elements than the other arrays but still realizes accurate beam scanning, thus offering a higher gain and a finer angular resolution, which is partially made possible by the efficient automatic calibration method.

5. Conclusions

In summary, this work reported the design and experimental validation of an integrated 1×16 K-band CP LCPA, together with its OTA calibration. Each channel of the LCPA includes a diagonally chamfered stacked patch antenna and an LCPS based on an LDL structure with 5 μm-thick ultrathin LCs, which can provide a maximum phase-shifting range of more than 360° and an FoM of 78.3°·dB^{-1}. Moreover, a near-field OTA automatic calibration based on the SEM was proposed and implemented to extract the phase–voltage curves of the 16 channels of the LCPA. A prototype of the fabricated LCPA was measured and was shown to provide a scanned CP beam covering from −40° to +40° with a peak gain of 12.5 dBic and a scanning loss of less than 2.5 dB. The bandwidth of the LCPA, which satisfies the requirements of a joint $|S_{11}|$ < −15 dB, AR < 3 dB, beam squinting < 3°, and gain variation < 2.2 dB, spans from 25.5 to 26.0 GHz. Compared with existing LCPAs, the proposed LCPA has the advantages of a high gain, high efficiency, low profile, and faster response time, making it potentially promising for millimeter-wave communications such as satellite communications and radar systems. The methodology presented here offers a systematic solution for LCPAs, which can be beneficial for the design and characterization of various types of beam-scanning arrays based on LCs and even on other phase-change materials.

Acknowledgments

This work was supported in part by the National Natural Science Foundation of China (NSFC; 62122019 and 62293492), the National Key Research and Development Program of China (2019YFB2204704), and the Fundamental Research Funds for the Central Universities and the Zhishan Scholar Program of Southeast University (2242022R40038). The authors thank Tianyi Huo for his assistance during the antenna measurements.

Compliance with ethics guidelines

Xinyu Wu, Fengshuo Wan, Hongyuan Feng, Shichao Jin, Chong Guo, Yu Wei, Dunge Liu, Yuqian Yang, Longzhu Cai, Zhihao Jiang, and Wei Hong declare that they have no conflict of interest and financial conflicts to disclose.

Appendix A. Supplementary material

Supplementary data to this article can be found online at https://doi.org/10.1016/j.eng.2023.08.013.

References

[1] Hong W, Jiang ZH, Yu C, Hou D, Wang H, Guo C, et al. The role of millimeter-wave technologies in 5G/6G wireless communications. IEEE J Microwaves 2021;1(1):101–22.
[2] Lin J, Yu W, Zhang N, Yang X, Zhang H, Zhao W. A survey on internet of things: architecture, enabling technologies, security and privacy, and applications. IEEE Internet Things J 2017;4(5):1125–42.

[3] Mailloux RJ. Phased array antenna handbook. 3rd ed. Boston: Artech House Publishers; 2018.
[4] Yin Y, Ustundag B, Kibaroglu K, Sayginer M, Rebeiz GM. Wideband 23.5–29.5-GHz phased arrays for multistandard 5G applications and carrier aggregation. IEEE Trans Microwave Theory Tech 2021;69(1):235–47.
[5] Kim JW, Chae SC, Jo HW, Yeo TD, Yu JW. Wideband circularly polarized phased array antenna system for wide axial ratio scanning. IEEE Trans Antennas Propag 2022;70(2):1523–8.
[6] Xiao S, Zheng C, Li M, Xiong J, Wang BZ. Varactor-loaded pattern reconfigurable array for wide-angle scanning with low gain fluctuation. IEEE Trans Antennas Propag 2015;63(5):2364–9.
[7] Ji Y, Ge L, Wang J, Chen Q, Wu W, Li Y. Reconfigurable phased-array antenna using continuously tunable substrate integrated waveguide phase shifter. IEEE Trans Antennas Propag 2019;67(11):6894–908.
[8] Cao YF, Zhang XY. A wideband beam-steerable slot antenna using artificial magnetic conductors with simple structure. IEEE Trans Antennas Propag 2018;66(4):1685–94.
[9] Topalli K, Civi OA, Demir S, Koc S, Akin T. A monolithic phased array using 3-bit distributed RF MEMS phase shifters. IEEE Trans Microwave Theory Tech 2008;56(2):270–327.
[10] Jung C, Lee M, Li GP, de Flaviis F. Reconfigurable scan-beam single-arm spiral antenna integrated with RF-MEMS switches. IEEE Trans Antennas Propag 2006;54(2):455–63.
[11] Nafe A, Ghaffar FA, Farooqui MF, Shamim A. A ferrite LTCC-based monolithic SIW phased antenna array. IEEE Trans Antennas Propag 2017;65(1):196–205.
[12] Karnati KK, Shen Y, Trampler ME, Ebadi S, Wahid PF, Gong X. A BST-integrated capacitively loaded patch for Ka- and X-band beamsteerable reflectarray antennas in satellite communications. IEEE Trans Antennas Propag 2015;63(4):1324–33.
[13] Karabey OH, Gaebler A, Strunck S, Jakoby R. A 2-D electronically steered phased-array antenna with 2 × 2 elements in LC display technology. IEEE Trans Microwave Theory Tech 2012;60(5):1297–306.
[14] Maune H, Jost M, Reese R, Polat E, Nickel M, Jakoby R. Microwave liquid crystal technology. Crystals 2018;8(9):355.
[15] Jakoby R, Gaebler A, Weickhmann C. Microwave liquid crystal enabling technology for electronically steerable antennas in SATCOM and 5G millimeter-wave systems. Crystals 2020;10(6):514.
[16] Stevenson R, Sazegar M, Bily A, Johnson M, Kundtz N. Metamaterial surface antenna technology: commercialization through diffractive metamaterials and liquid crystal display manufacturing. In: Proceedings of 2016 10th International Congress on Advanced Electromagnetic Materials in Microwaves and Optics (METAMATERIALS); 2016 Sep 19–22; Chania, Greece. Piscataway: IEEE; 2016. p. 349–51.
[17] Yang DK, Wu ST. Fundamentals of liquid crystal devices. 2nd ed. Hoboken: John Wiley & Sons, Inc.; 2014.
[18] Goelden F, Gaebler A, Goebel M, Manabe A, Mueller S, Jakoby R. Tunable liquid crystal phase shifter for microwave frequencies. Electron Lett 2009;45(13):686–7.
[19] Bulja S, Mirshekar-Syahkal D. Meander line millimetre-wave liquid crystal based phase shifter. Electron Lett 2010;46(11):769–71.
[20] Wang D, Polat E, Schuster C, Tesmer H, Rehder GP, Serrano ALC, et al. Fast and miniaturized phase shifter with excellent figure of merit based on liquid crystal and nanowire-filled membrane technologies. IEEE J Microwaves 2022;2(1):174–84.
[21] Kamrath F, Polat E, Matic S, Schuster C, Miek D, Tesmer H, et al. Bandwidth and center frequency reconfigurable waveguide filter based on liquid crystal technology. IEEE J Microwave 2022;2(1):134–44.
[22] Polat E, Kamrath F, Matic S, Tesmer H, Jiménez-Sáez A, Wang D, et al. Novel hybrid electric/magnetic bias concept for tunable liquid crystal based filter. IEEE J Microwaves 2022;2(3):490–5.
[23] Karabey OH, Bildik S, Bausch S, Strunck S, Gaebler A, Jakoby R. Continuously polarization agile antenna by using liquid crystal-based tunable variable delay lines. IEEE Trans Antennas Propag 2013;61(1):70–6.
[24] Shu J, Zhang Y. Design of a liquid crystal beam-steerable antenna with characteristic mode analysis. IET Microwaves Antennas Propag 2022;16(1):29–36.
[25] Tesmer H, Reese R, Polat E, Nickel M, Jakoby R, Maune H. Liquid-crystal-based fully dielectric lateral wave beam-steering antenna. IEEE Antennas Wireless Propag Lett 2019;18(12):2577–81.
[26] Reese R, Jost M, Polat E, Tesmer H, Strobl J, Schuster C, et al. A millimeter-wave beam-steering lens antenna with reconfigurable aperture using liquid crystal. IEEE Trans Antennas Propa 2019;67(8):5313–24.
[27] Stevenson RA, Fotheringham D, Freeman T, Noel T, Mason T, Shafie S. High-throughput satellite connectivity for the constant contact vehicle. In: Proceedings of 2018 48th European Microwave Conference (EuMC); 2018 Sep 23–27; Madrid, Spain. Piscataway: IEEE; 2018. p. 316–9.
[28] Zhang W, Li Y, Zhang Z. A reconfigurable reflectarray antenna with an 8 μm-thick layer of liquid crystal. IEEE Trans Antennas Propag 2022;70(4):2770–8.
[29] Li X, Wan Y, Liu J, Jiang D, Bai T, Zhu K, et al. Broadband electronically scanned reflectarray antenna with liquid crystals. IEEE Antennas Wireless Propag Lett 2021;20(3):396–400.
[30] Perez-Palomino G, Baine P, Dickie R, Bain M, Encinar JA, Cahill R, et al. Design and experimental validation of liquid crystal-based reconfigurable reflectarray elements with improved bandwidth in F-band. IEEE Trans Antennas Propag 2013;61(4):1704–13.
[31] Li XY, Jiang D, Liu J, Tong MS. A Ka-band multilayer beaming-scanning antenna using liquid crystals. IEEE Antennas Wireless Propag Lett 2022;21(1):44–8.
[32] Shu J, Xu G, Peng H, Mao J. An electrically steerable parasitic array radiator in package based on liquid crystal. IEEE Antennas Wireless Propag Lett 2019;18(11):2365–9.
[33] Ma S, Zhang SQ, Ma LQ, Meng FY, Erni D, Zhu L, et al. Compact planar array antenna with electrically beam steering from backfire to endfire based on liquid crystal. IET Microwaves Antennas Propag 2018;12(7):1140–6.
[34] Karabey OH, Mehmood A, Ayluctarhan M, Braun H, Letz M, Jakoby R. Liquid crystal based phased array antenna with improved beam scanning capability. Electron Lett 2014;50(6):426–8.
[35] Wang D, Polat E, Tesmer H, Jakoby R, Maune H. A compact and fast 1 × 4 continuously steerable endfire phased-array antenna based on liquid crystal. IEEE Antennas Wireless Propag Lett 2021;20(10):1859–62.
[36] Panahi A, Yeung L, Hedayati M, Wang YE. Sub-6 GHz high FOM liquid crystal phase shifter for phased array antenna. IEEE J Microwaves 2022;2(2):316–25.
[37] Wang D, Polat E, Tesmer H, Maune H, Jakoby R. Switched and steered beam end-fire antenna array fed by wideband via-less butler matrix and tunable phase shifters based on liquid crystal technology. IEEE Trans Antennas Propag 2022;70(7):5383–92.
[38] Mano S, Katagi T. A method for measuring amplitude and phase of each radiating element of a phased array antenna. Electron Commun Jpn 1982;65(5):58–64.
[39] Takahashi T, Konishi Y, Makino S, Ohmine H, Nakaguro H. Fast measurement technique for phased array calibration. IEEE Trans Antennas Propag 2008;56(7):1888–99.
[40] Lee KM, Chu RS, Liu SC. A built-in performance-monitoring/fault isolation and correction (PM/FIC) system for active phased-array antennas. IEEE Trans Antennas Propag 1993;41(11):1530–40.
[41] Keizer WPMN. Fast and accurate array calibration using a synthetic array approach. IEEE Trans Antennas Propag 2011;59(11):4115–22.
[42] Kianinejad A, Chen ZN, Qiu CW. Design and modeling of spoof surface plasmon modes-based microwave slow-wave transmission line. IEEE Trans Microwave Theory Tech 2015;63(6):1817–25.
[43] Gevorgian S. Ferroelectrics in microwave devices, circuits and systems: physics, modeling, fabrication and measurements. Berlin: Springer; 2009.
[44] Gao H, Wang W, Wu Y, Liu Y, Pedersen GF, Fan W. Experimental comparison of on–off and all-on calibration modes for beam-steering performance of mmWave phased array antenna-in-package. IEEE Trans Instrum Meas 2021;70:8002509.
[45] Fitzgibbon A, Pilu M, Fisher RB. Direct least square fitting of ellipses. IEEE Trans Pattern Anal Mach Intell 1999;21(5):476–80.
[46] Kim TW, Park JS, Park SO. A theoretical model for resonant frequency and radiation pattern on rectangular microstrip patch antenna on liquid crystal substrate. IEEE Trans Antennas Propag 2018;66(9):4533–40.
[47] Bulja S, Mirshekar-Syahkal D, James R, Day E, Fernández FA. Measurement of dielectric properties of nematic liquid crystals at millimeter wavelength. IEEE Trans Microwave Theory Tech 2010;58(12):3493–501.
[48] Brown AD. Electronically scanned arrays MATLAB® modeling and simulation. Boca Rato: CRC Press; 2017.
[49] Cameron RJ, Chandra MK, Raafat RM. Microwave filters for communication systems: fundamentals, design, and applications. Hoboken: John Wiley & Sons, Inc.; 2018.